Collective durotaxis along a self-generated stiffness gradient *in vivo*

Adam Shellard[1] and Roberto Mayor[1]*

[1]*Department of Cell and Developmental Biology, University College London, Gower Street, London WC1E 6BT, UK*

*Corresponding author. Correspondence and request for materials should be addressed to R.M. (Email: r.mayor@ucl.ac.uk)

Abstract

Collective cell migration underlies morphogenesis, wound healing, and cancer invasion[1,2]. Most directed migration *in vivo* has been attributed to chemotaxis, in which cells follow a chemical gradient[3-5]. Cells can also follow a stiffness gradient *in vitro*, a process called durotaxis[3,4,6-8], but evidence for durotaxis *in vivo* is scarce[6]. Here we found that the neural crest, an embryonic cell population, self-generates a stiffness gradient in the adjacent placodal tissue, and follows this gradient by durotaxis. The gradient moves with the neural crest, which are continually pursuing a retreating region of high substrate stiffness. Mechanistically, the neural crest induces the gradient due to N-Cadherin interactions with the placodes and senses the gradient via cell-matrix adhesions, resulting in polarised Rac activity and actomyosin contractility, which coordinates durotaxis. Durotaxis synergises with chemotaxis, cooperatively polarising the cell group's actomyosin machinery to prompt efficient directional collective cell migration *in vivo*. These results show that durotaxis and dynamic stiffness gradients exist *in vivo*, and gradients of chemical and mechanical signals cooperate to achieve efficient directional cell migration.

Collective cell migration is essential for morphogenesis, tissue remodelling and cancer invasion[1,2]. Most cell migration *in vivo* is directional, with cells guided by extracellular signals[1,3,4]. Chemotaxis, the well-established process whereby cells follow gradients of soluble chemical cues, is the main mechanism proposed to direct cell migration *in vivo*[1,3-5]. Extracellular mechanics are now also believed to contribute to cell guidance[9]. Some cell types can individually or collectively follow gradients in the stiffness of their substrate, a process known as durotaxis[3,4,6-9]. However, although stiffness of biological tissues inevitably presents heterogeneities[10], difficulties of accessing, measuring and manipulating stiffness *in vivo* have meant there is still scarce evidence that durotaxis occurs *in vivo*, despite more than 20 years passing since its discovery *in vitro*[6,7]. Moreover, it is unclear how a stiffness gradient can be formed *in vivo* and how gradients of chemical and mechanical cues might interplay in the complex 3D *in vivo* environment to coordinate directional cell migration.

A dynamic substrate stiffness gradient

The neural crest is an embryonic stem cell population that originates in the dorsal aspect of the neural tube and collectively migrates long distances through the embryo. Recent work using *Xenopus laevis* embryos demonstrating that mechanical stiffening of the mesoderm is essential for initiating their migration[11] led us to ask whether the direction of neural crest migration is controlled by cells following a stiffness gradient (durotaxis) *in vivo*. We have previously shown that neural crest cells are engaged in a “chase-and-run” behaviour with the adjacent cranial placodes (Fig 1a; Extended Data Fig. 1a-c, e). The cranial placodes are the source of the chemoattractant Sdf1, which causes neural crest to undergo chemotaxis toward the placodes (“chase”)[12] (Fig. 1a; Extended Data Fig. 1c); however, once the neural crest reaches the placode they are engaged in an N-Cadherin-dependent repulsive behaviour, which makes the placodes move away from the neural crest (“run”) (Fig. 1a; Extended Data Fig. 1e)[12]. This “chase-and-run” leads to the placodes moving ahead of the neural crest[12-14]. Here we identified fibronectin – the only extracellular matrix component used for neural crest migration – at the interface between the two tissues (Fig. 1b; Extended Data Fig. 1c-f), being more abundant at this interface than at the neural crest’s interface with the underlying mesoderm[15] (Extended Data Fig. 1g-i), suggesting that the placode represent the major substrate for neural crest

migration, and that the neural crest is mechanosensitive to the placode. To investigate the mechanical properties of the placode, we removed the superficial ectoderm and measured the apparent elasticity by nanoindentation on the placodes (Extended Data Fig. 2a-c). Prior to neural crest migration, the placodal substrate along the presumptive path exhibits a uniform stiffness, whereas a stiffness gradient emerges as the neural crest begins migrating (Fig. 1c; Extended Data Fig. 2d-g), which coincides with extensive interactions between the neural crest and placodes (Fig. 1b; Extended Data Fig. 1e, f). Ablation or impaired formation of the placodes through injection of an Eya1 morpholino (Extended Data Fig. 2h, i) resulted in loss off the stiffness gradient (Fig. 1d) and impaired neural crest migration (Extended Data Fig. 2j), confirming that the stiffness gradient represents the placodal tissue. Furthermore, the length of the cranial placodes matched the length of the stiffness gradient measured (Extended Data Fig. 2k). Together, these observations indicate that there is a stiffness gradient in the placode tissue.

The placodes move as consequence of a “chase-and-run” interaction with neural crest[20], which suggests that the stiffness gradient may move as the neural crest migrate. We found that the stiffness gradient is robust throughout neural crest migration and retreats as the neural crest migrate forward, meaning the neural crest chase a retreating region of high stiffness (Fig. 1e; Extended Data Fig. 2l, m). Mesoderm underlying the neural crest during these stages exhibits uniform stiffness along the migratory axis and is comparatively soft (Extended Data Fig. 2n)[11], suggesting that lower forces are applied by the neural crest on the mesoderm than on the placodes[16], which further supports the idea that the placode represent the major substrate for the neural crest during migration. Together, these data suggest that a stiffness gradient emerges across the placodal tissue as the neural crest migrate.

A self-generated stiffness gradient

The fact that the gradient emerges at the onset of – and persists during – neural crest migration, suggests that the migratory neural crest cells themselves are generating the stiffness gradient. To investigate this hypothesis, we measured the stiffness of embryos in which neural crest had been ablated or where neural crest formation was specifically impaired through injection of a Twist morpholino

(Extended Data Fig. 3a) Both treatments led to loss of neural crest (Extended Data Fig. 3b) and the stiffness gradient was not formed (Fig. 1f). To test the capacity of neural crest to self-generate the placodal stiffness gradient, we grafted neural crest at the opposite side of the placodes in the ventral region of the embryo, where no stiffness gradient is present (Fig. 1g; Extended Data Fig. 3c). Such grafts resulted in the induction of an ectopic stiffness gradient of reversed orientation (Fig. 1h).

We next questioned the molecular basis for the formation of a self-generated gradient. We have previously shown that N-Cadherin-based interactions between neural crest cells and placode cells are important for the "chase-and-run" behaviour[12] (Extended Data Fig. 3d), and emerge at the onset of neural crest migration, coincident with the formation of the stiffness gradient, which suggests that this interaction might facilitate local placodal softening as a means of gradient generation. To test the hypothesis that softening of placodes depends on N-cadherin engagement we explanted placodes onto substrates of either fibronectin alone or fibronectin and N-Cadherin together (Extended Data Fig. 3e). N-Cadherin was sufficient to reduce placodal stiffness (Fig. 1i) and disrupt the actin cytoskeleton (Fig. 1j, k). To further investigate the role of N-cadherin *in vivo*, we injected embryos with a N-Cadherin morpholino. As expected, inhibition of N-cadherin resulted in loss of the stiffness gradient with the consequent failure in neural crest migration (Fig. 1l-n; Extended Data Fig. 3f). We have previously shown that local indentation increases the stiffness of tissues[11]. We found that this technique also produces an exogeneous stiffness gradient (Extended Data Fig. 3g, h) and was able to rescue neural crest migration after N-Cadherin knockdown (Fig. 1l-n; Extended Data Fig. 3f). Altogether, these results show that the neural crest self-generates a stiffness gradient by directly interacting with placode cells through N-Cadherin, and that this gradient is required for neural crest durotaxis *in vivo*.

Neural crest durotaxis *in vivo*

To further confirm that neural crest undergoes durotaxis *in vivo* we abrogated the stiffness gradient by mechanical ablation of ectodermal tissue away from the neural crest (Fig. 2a). Such ablation was able to completely abrogate the stiffness gradient (Fig. 2b), resulting in impaired neural crest migration (Fig. 2c, d), in which the cells underwent random movement, rather than directional migration, indicating that the

stiffness gradient impacts directionality rather than motility in general (Fig. 2e-h; Extended Data Fig. 4a, b; Supplementary Videos 1, 2). These observations demonstrate that durotaxis is necessary for neural crest migration *in vivo*.

Rac and actomyosin polarity in durotaxis

To understand the mechanism by which neural crest cells sense and respond to the stiffness gradient, we used an *in vitro* system where external cues such as chemical and mechanical gradients can be more easily controlled. Neural crest cells cultured on polyacrylamide gel substrates exhibiting stiffness gradients underwent highly efficient long-range collective durotaxis (Extended Data Fig. 4c-n and Supplementary Video 3).

We have previously shown that chemotaxis is powered by polarised actomyosin contraction[17] and actomyosin contraction is known to be an important component of the mechanical response to stiffness gradients[8]. Live imaging of neural crest revealed that, in agreement with previous findings[17], clusters exhibit a contractile actomyosin cable at its edge *in vivo* and *ex vivo* on stiffness gradients (Fig. 3a; Extended Data Fig. 5a-d). Although the dynamics of actomyosin contraction were unaffected by external gradients (Extended Data Fig. 5e, f), contractility was polarised in clusters on chemical or mechanical gradients (Fig. 3b), with this polarity predicting cluster movement (Extended Data Fig. 5g, h), suggesting that rear contraction might be necessary for directed migration. To test the requirement of myosin contractility for collective cell durotaxis, we incubated explants with the myosin II inhibitor, blebbistatin, which resulted in a failure of explants to undergo directional migration on stiffness gradients (Extended Data Fig. 5i, j). Likewise, laser ablation of the actomyosin cable at the rear of neural crest clusters inhibited durotaxis (Fig. 3c-e; Extended Data Fig. 5k-m).

To understand the mechanism by which actomyosin contraction is polarised in neural crest exposed to a stiffness gradient, we investigated the localisation of active Rac, which is known to be mutually antagonistic with a stimulator of actomyosin contraction, RhoA[17,18]. Rac1-GTP was polarised in explants on stiffness gradients, with more active Rac at the front compared to the rear (Fig. 3f, g). Rac-GTP was polarised in both front and rear cells at the single cell level (Extended Data Fig. 6a, b), consistent with previous observations that show Rac-GTP is polarised toward the

cluster edge independent of external cues[19]. The sensing module likely responsible for this are integrins, present in cell-matrix adhesions, which are mechanosensitive and activate Rac1[20]; indeed, by immunostaining vinculin we observed a polarised distribution of cell-matrix adhesions in durotactic clusters (Extended Data Fig. 6c, d). Furthermore, knockdown of integrin β1 caused Rac1 activity to be lost (Extended Data Fig. 6e, f), supporting the notion that stiffer substrates lead to higher levels of Rac1 in an integrin-dependent manner, a mechanism which is likely a general feature of neural crest migration. Altogether, these data suggest that neural crest collectives respond to a stiffness gradient by generating a supracellular polarity of cell-matrix adhesions, Rac and actomyosin contractility to undergo durotaxis, similar to the chemotaxis mechanism[17].

Durotaxis-chemotaxis synergy

The fact that neural crest undergo chemotaxis and durotaxis suggest that there may be interplay between chemical and mechanical gradients to control cell migration *in vivo*. Morpholino-mediated knockdown of Sdf1 inhibited neural crest migration[19], which was rescued by placement of an Sdf1-coated bead along the normal route of the neural crest (Fig. 4a, b; Extended Data Fig. 7a). This rescue was disrupted by inhibition of the stiffness gradient, demonstrating that chemotaxis is durotaxis-dependent *in vivo* (Fig. 4a, b; Extended Data Fig. 7a, b). We then tested the sufficiency of chemotactic and durotactic cues to direct collective cell migration *in vivo*. We have previously shown that Sdf1 beads can induce neural crest to move outside their normal routes when a stiffness gradient pre-exists[19]. To test whether the neural crest could be forced to move to a truly ectopic location, we placed an Sdf1-coated bead, and locally indented, into a region opposite the normal migratory route to induce ectopic chemotactic and durotactic gradients, respectively, which were steeper than the endogenous gradients. Either gradient alone was insufficient to produce ectopic migration but combining exogeneous chemotactic and durotactic gradients together was sufficient to induce ectopic neural crest migration in the opposite direction to the normal migratory route (Fig. 4c, d; Extended Data Fig. 7e-l). These data demonstrate that durotaxis cooperates with chemotaxis *in vivo* to direct neural crest migration.

To analyse the interaction between durotaxis and chemotaxis in detail, we analysed neural crest behaviour in a controlled *ex vivo* system. We fabricated polyacrylamide gel substrates exhibiting either uniform stiffness or a stiffness gradient with similar stiffness values to those measured *in vivo* (Extended Data Fig. 8a, b) and coated with fibronectin (Extended Data Fig. 8c-f)[15]. Neural crest exposed to physiological graded stiffness underwent inefficient collective durotaxis *ex vivo* compared to their normal migration *in vivo* (Fig. 4e, f; Extended Data Fig. 9a-d, i). This behaviour could not be explained by differences in the absolute stiffness of the substrate because neural crest migrated with similar efficiency on different portions of the gel (Extended Data Fig. 8g). Interestingly, although the amount of active Rac was a function of the absolute stiffness, Rac polarity was maintained irrespective of the position of the explants on the gradient, which may explain why durotaxis exhibits similar efficient on all portions of the gradient gel (Extended Data Fig. 8h-j). Likewise, explants on gels with stiffness equivalent to the stiffness found by neural crest at the beginning of its migration, underwent inefficient chemotaxis to Sdf1 (Fig. 4e, f; Extended Data Fig. 9e, f, i). By contrast, neural crest exposed to gradients of Sdf1, and stiffness simultaneously underwent efficient directional migration (Fig. 4e, f; Extended Data Fig. 9g-i), an effect that was synergistic (Extended Data Fig. 9j-m) and comparable to the migration observed *in vivo* (Fig. 4e, f). Interestingly, single cells were incapable of undergoing durotaxis on physiological stiffness gradients (Extended Data Fig. 9n-p), suggesting that durotaxis is an emergent property of collectiveness, similar to the results of a previous study[7]. Synergy between durotaxis and chemotaxis may operate through actomyosin contraction, which is regulated by both. Neural crest clusters exposed to chemical and mechanical gradients simultaneously exhibited more polarised actomyosin contraction compared to either gradient alone and this polarity scaled non-linearly with the efficiency of migration (Fig. 4g, h; Extended Data Fig. 10). Altogether, these data suggest that chemical and mechanical signals act on a common subset of cellular components to cooperatively control cell migration.

Discussion

We show here evidence for collective durotaxis *in vivo*. The heterogeneity and dynamics of stiffness changes *in vivo* during development and disease[10,21,22] suggests that durotaxis may be a widespread phenomenon *in vivo*. Although

durotaxis is more efficient on steeper gradients, our data support previous observations that cells are nonetheless capable of undergoing durotaxis on physiological gradients[23], suggesting that durotaxis may be more common in development and homeostasis than previously though.

Our data show that the neural crest follows two gradients generated by the cranial placodes: a chemical gradient, from Sdf1 secretion, along with a stiffness gradient that is self-generated by the migratory neural crest cells (Fig. 4i)[12,19]. This may act as a robust long-range guidance cue, in a conceptually analogous manner to self-generated chemotactic gradients[24,25], and reveal an alternative to externally generated stiffness gradients, like in the case of axon growth in the developing eye which grows toward softer tissues based on differential cell proliferation of the underlying tissue[21,26].

There is previous evidence that the underlying mesoderm is also mechanically sensed by the neural crest[11]. Combined, these data suggest that neural crest integrate mechanical signals from both surrounding tissues, in which stiffness of the mesoderm promotes cell motility by activating the epithelial-to-mesenchymal transition (EMT) genetic cascade[11], whereas gradients of the placode guide the direction of neural crest movement. The fact that the mesoderm is stationary and spans the entire neural crest path may mean it can provide constant reinforcement of neural crest remaining motile, whereas the moving placode allows it to dynamically provide directionality[12].

Both chemical and mechanical gradients result in a supracellular polarisation of Rac and actomyosin contraction, which drives efficient collective cell migration, likely in concert with focal adhesion ‘tugging’ to sense substrate rigidity[27]. In other contexts, different types of gradients may cooperate and compete to dictate cell motion[3].

Competing interests

The authors declare no competing interests.

Acknowledgments

We thank G. Charras for the PDMS and useful discussions, J. Hartmann for assistance with calculating synergy statistics, E. Theveneau for gifting the Eya1 and Foxi1c probes, M. Klymkowsky for gifting the Sox3 antibody, and E. Barriga for preliminary experiments. We thank G. Charras, B. Stramer and J. Hartmann for comments on the manuscipt. We thank the anonymous reviewers for their contribution to the peer review of this work. Work in RM laboratory is supported by grants from the Medical Research Council (MR/S007792/1), Biotechnology and Biological Sciences Research Council (M008517, BB/T013044) and Wellcome Trust (102489/Z/13/Z).

Author contributions

A.S. and R.M. conceived the project and designed the experiments. A.S. performed and analysed all the experiments. R.M. contributed to experimental repeats and analysis of the data in Fig. 1c, Fig. 2b, e. A.S. and R.M. wrote and edited the manuscript.

1 Yamada, K. M. & Sixt, M. Mechanisms of 3D cell migration. *Nature Reviews Molecular Cell Biology* **20**, 738-752, doi:10.1038/s41580-019-0172-9 (2019).

2 Friedl, P. & Gilmour, D. Collective cell migration in morphogenesis, regeneration and cancer. *Nature Reviews Molecular Cell Biology* **10**, 445-457, doi:10.1038/nrm2720 (2009).

3 Shellard, A. & Mayor, R. All Roads Lead to Directional Cell Migration. *Trends in Cell Biology* **30**, 852-868, doi:10.1016/j.tcb.2020.08.002 (2020).

4 SenGupta, S., Parent, C. A. & Bear, J. E. The principles of directed cell migration. *Nature Reviews Molecular Cell Biology* **22**, 529-547, doi:10.1038/s41580-021-00366-6 (2021).

5 Insall, R. H. Understanding eukaryotic chemotaxis: a pseudopod-centred view. *Nature Reviews Molecular Cell Biology* **11**, 453-458, doi:10.1038/nrm2905 (2010).

6 Shellard, A. & Mayor, R. Durotaxis: The Hard Path from In Vitro to In Vivo. *Developmental Cell* **56**, 227-239, doi:10.1016/j.devcel.2020.11.019 (2021).

7 Lo, C. M., Wang, H. B., Dembo, M. & Wang, Y. L. Cell movement is guided by the rigidity of the substrate. *Biophysical Journal* **79**, 144-152, doi:10.1016/s0006-3495(00)76279-5 (2000).

8 Sunyer, R. *et al.* Collective cell durotaxis emerges from long-range intercellular force transmission. *Science* **353**, 1157-1161, doi:10.1126/science.aaf7119 (2016).

9 Charras, G. & Sahai, E. Physical influences of the extracellular environment on cell migration. *Nature Reviews Molecular Cell Biology* **15**, 813-824, doi:10.1038/nrm3897 (2014).

10 Guimaraes, C. F., Gasperini, L., Marques, A. P. & Reis, R. L. The stiffness of living tissues and its implications for tissue engineering. *Nature Reviews Materials* **5**, 351-370, doi:10.1038/s41578-019-0169-1 (2020).

11 Barriga, E. H., Franze, K., Charras, G. & Mayor, R. Tissue stiffening coordinates morphogenesis by triggering collective cell migration in vivo. *Nature* **554**, 523-+, doi:10.1038/nature25742 (2018).

12 Theveneau, E. *et al.* Chase-and-run between adjacent cell populations promotes directional collective migration. *Nature Cell Biology* **15**, 763-+, doi:10.1038/ncb2772 (2013).

13 Szabo, A. & Mayor, R. Mechanisms of Neural Crest Migration. *Annual Review of Genetics, Vol 52* **52**, 43-63, doi:10.1146/annurev-genet-120417-031559 (2018).

14 Shellard, A. & Mayor, R. Chemotaxis during neural crest migration. *Seminars in Cell & Developmental Biology* **55**, 111-118, doi:10.1016/j.semcdb.2016.01.031 (2016).

15 Alfandari, D., Cousin, H., Gaultier, A., Hoffstrom, B. G. & DeSimone, D. W. Integrin alpha 5 beta 1 supports the migration of Xenopus cranial neural crest on fibronectin. *Developmental Biology* **260**, 449-464, doi:10.1016/s0012-1606(03)00277-x (2003).

16 Schiller, H. B. *et al.* beta(1)- and alpha(v)-class integrins cooperate to regulate myosin II during rigidity sensing of fibronectin-based microenvironments. *Nature Cell Biology* **15**, 625-+, doi:10.1038/ncb2747 (2013).

17 Shellard, A., Szabo, A., Trepat, X. & Mayor, R. Supracellular contraction at the rear of neural crest cell groups drives collective chemotaxis. *Science* **362**, 339-+, doi:10.1126/science.aau3301 (2018).

18 Guilluy, C., Garcia-Mata, R. & Burridge, K. Rho protein crosstalk: another social network? *Trends in Cell Biology* **21**, 718-726, doi:10.1016/j.tcb.2011.08.002 (2011).

19 Theveneau, E. *et al.* Collective Chemotaxis Requires Contact-Dependent Cell Polarity. *Developmental Cell* **19**, 39-53, doi:10.1016/j.devcel.2010.06.012 (2010).

20 Wang, S. J. *et al.* Tiam1 interaction with the PAR complex promotes talin-mediated Rac1 activation during polarized cell migration. *Journal of Cell Biology* **199**, 331-345, doi:10.1083/jcb.201202041 (2012).

21 Koser, D. E. *et al.* Mechanosensing is critical for axon growth in the developing brain. *Nature Neuroscience* **19**, 1592-1598, doi:10.1038/nn.4394 (2016).

22 Zhu, M. *et al.* Spatial mapping of tissue properties in vivo reveals a 3D stiffness gradient in the mouse limb bud. *Proceedings of the National Academy of Sciences of the United States of America* **117**, 4781-4791, doi:10.1073/pnas.1912656117 (2020).
23 Tse, J. R. & Engler, A. J. Stiffness Gradients Mimicking In Vivo Tissue Variation Regulate Mesenchymal Stem Cell Fate. *Plos One* **6**, doi:10.1371/journal.pone.0015978 (2011).
24 Tweedy, L. *et al.* Seeing around corners: Cells solve mazes and respond at a distance using attractant breakdown. *Science* **369**, 1075-+, doi:10.1126/science.aay9792 (2020).
25 Dona, E. *et al.* Directional tissue migration through a self-generated chemokine gradient. *Nature* **503**, 285-+, doi:10.1038/nature12635 (2013).
26 Thompson, A. J. *et al.* Rapid changes in tissue mechanics regulate cell behaviour in the developing embryonic brain. *Elife* **8**, doi:10.7554/eLife.39356 (2019).
27 Plotnikov, S. V., Pasapera, A. M., Sabass, B. & Waterman, C. M. Force Fluctuations within Focal Adhesions Mediate ECM-Rigidity Sensing to Guide Directed Cell Migration. *Cell* **151**, 1513-1527, doi:10.1016/j.cell.2012.11.034 (2012).

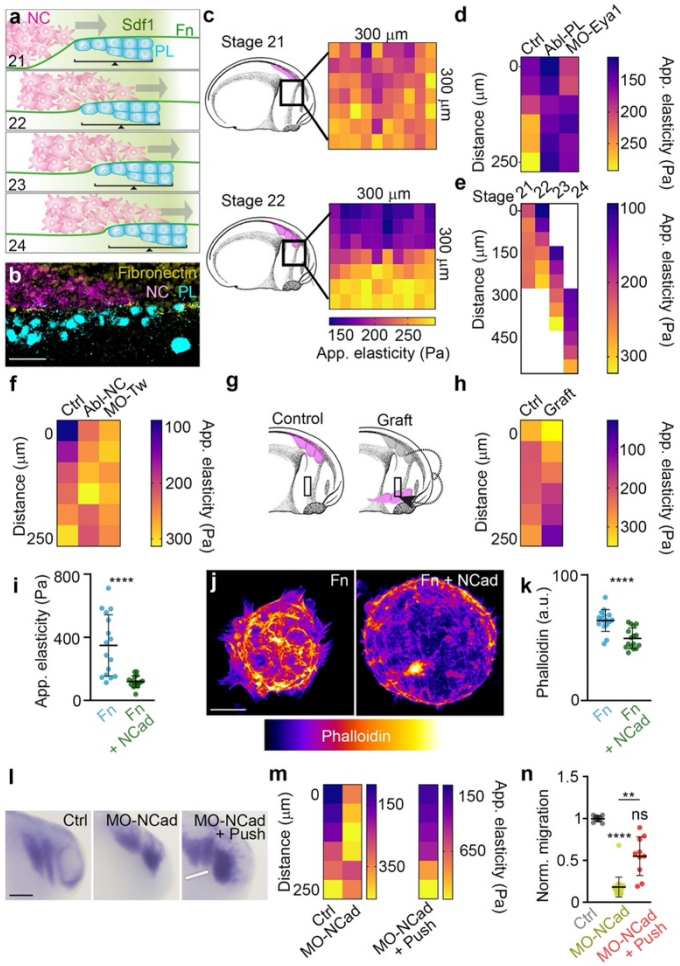

Figure 1. A dynamic self-generated stiffness gradient *in vivo*. a, Neural crest (NC, pink) engaged in "chase and run"[12] interaction with placodes (PL, blue). Neural crest chemotax toward Sdf1-secreting placode (Sdf1, green). The two cell types interact causing placode to run away. Grey arrows indicate movement of neural crest and/or placode. Developmental stage in bottom left. **b**, A cryosection showing *in situ* hybridisation for Twist (neural crest, magenta), and immunostaining for Sox3 (placodes, cyan) and fibronectin (yellow). Scale bar is 50 µm. **c**, Schematics of embryos prior (st. 21) to or at the start (st. 22) of neural crest (pink) migration. Black box: placode region in which the apparent elasticity was measured. **d**, Stiffness measurements after loss of placodes by ablation (Abl-PL) or morpholino injection of Eya1 (MO-Eya1). **e**, Stiffness measurements of the placodes over time (x-axis, stages indicated at the top) and space (distance 0 µm represent position of neural crest at st. 21; y-axis), as indicated in **a** (bracket). Note that the position of the stiffness gradient moves spatially as placode move in front of the neural crest. **f**, Stiffness measurements in the placodes after loss of neural crest by ablation (Abl-NC) or injection of Twist morpholino (MO-Tw). **g-h**, Schematics showing neural crest graft and the region in which stiffness was measured (black boxes; g), stiffness values (h). **i-k**, Placodes were cultured on fibronectin alone or with N-Cadherin. (i) Stiffness, (j) Phalloidin, (k) Phalloidin Quantification. Scale bar is 50 µm (j). **l-n**. Embryos injected with an N-Cadherin morpholino (MO-NCad) and pushed (l, grey rod) in a ventral region ahead of the neural crest. (l) ISH against *Slug*, (m) stiffness, and (n) migration. Scale bar is 200 µm (l). Diagrams in **c, g** are adapted from *Normal table of Xenopus laevis (Daudin)*. Copyright © 1994, Nieuwkoop and Faber. Reproduced by permission of Taylor and Francis books US. Statistics and reproducibility are in the source data and Methods.

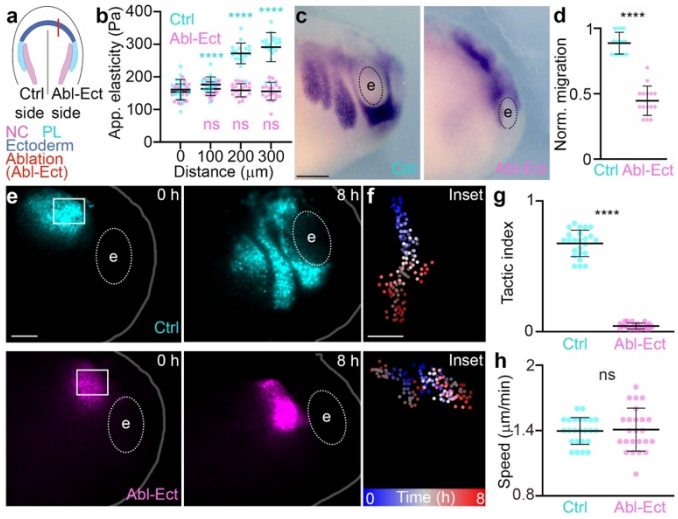

Figure 2. Neural crest durotaxis *in vivo*. a-d, Schematic of the dorsal view of a *Xenopus* embryo. The red line indicates the area of ectodermal relaxation by ablation (Abl-Ect), which is away from the neural crest and placodes; Stiffness measurements (b), *in situ* hybridisation for the neural crest marker, *Twist*; e: eye (c); neural crest migration (d). Scale bar is 200 µm (c). **e-h**, Graft of fluorescently labelled neural crest into control (cyan) or ablated (magenta) embryos (e), time-coded projected cell tracks (f), tactic index (g) and speed (h). Scale bar is 150 µm (e), 50 µm (f). Thick bars (b, d, g, h) represent mean, error bars (b, d, g, h) represent s.d.; Tukey's test (a), two-tailed Mann-Whitney *U* test (d, h), unpaired two-tailed *t*-test (g); ns, $P>0.05$, ****$P\leq0.0001$; $n = 20$ (b), 15 (d) embryos, 24 (g, h) cells. Statistics and reproducibility are in the source data and Methods.

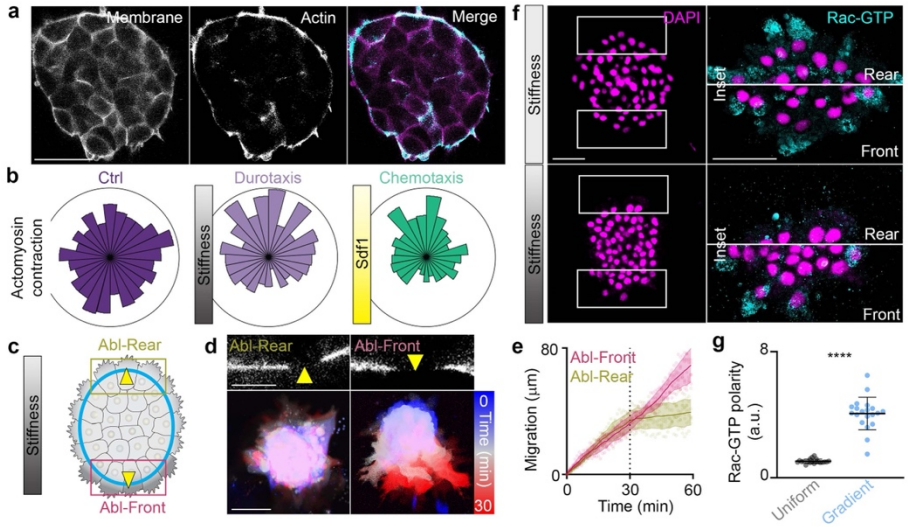

Figure 3. Polarised actomyosin contraction and Rac during durotaxis. a, Neural crest expressing fluorescently tagged LifeAct and membrane marker. Scale bar is 50 µm. **b**, Histograms representing the locations of actomyosin contraction during migration. **c-e**, Diagram (c) indicating actomyosin cable ablation (yellow arrowheads), LifeAct images of cable being ablated (d, top) at the rear (Abl-Rear) and front (Abl-Front) of neural crest clusters on a stiffness gradient, time-coded projection of clusters (d, bottom) in each condition, and quantification of migration (e). The dashed line (e) indicates the start of ablations. Scale bar is 10 µm (d, top), 100 µm (d, bottom). **f-g**, Immunostaining of Rac-GTP and DAPI in explants on uniform stiffness (f, top) or a stiffness gradient (f, bottom), and quantification of Rac-GTP

polarity (g). Scale bar is 50 µm (f). Thick bars represent (e, g) mean, error bars (e, g) represent s.d.; two-tailed Mann-Whitney *U* test (g); ****$P \leq 0.0001$; *n* = 500 (b, control), *n* = 600 (b, durotaxis, chemotaxis) contractions, *n* = 6 (e), 20 (g) explants. Statistics and reproducibility are in the source data and Methods.

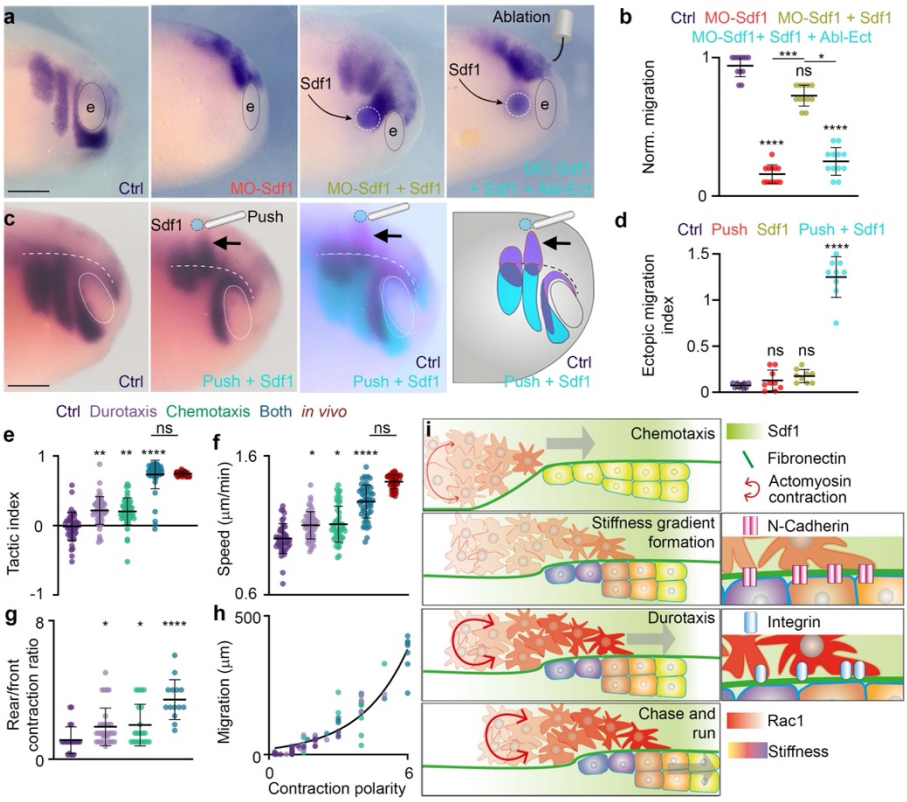

Figure 4. Durotaxis and chemotaxis cooperatively coordinate neural crest migration. a-b, Embryos stained by *in situ* hybridisation for the neural crest marker, *Slug*, when injected with a morpholino against Sdf1 (MO-Sdf1), inserted with a Sdf1-coated bead, and ablated to abrogate the stiffness gradient (Abl-Ect) (a) and migration quantified (b). Scale bar is 200 µm (a). **c-d**, Embryos stained for *Slug* (c, left) when inserted with a Sdf1-coated bead and locally pushed, pseudocolored overlap between the two sides of the embryo (c, middle), illustrative diagram (c, right) and quantification of ectopic migration (d). Scale bar is 200 µm (c). **e-f**, Tactic index (e) and speed (f). **g-h**, Quantification of the rear/front polarity of actomyosin contractions along the gradient axis (g) and correlation of migration with this polarity strength (h). **i**, Model of neural crest self-generated stiffness gradient and durotaxis. Neural crest in red, placodes in yellow (no stiffness gradient) or in purple (stiff) to yellow (soft) gradient (stiffness gradient). Thick bars (b, d-g) represent mean or a non-linear fit of correlation (h, $R^2 = 0.8704$); error bars (b, d-g) represent s.d.; Dunn's test (b, e-g), Tukey's test (d); ns, $P > 0.05$, *$P \leq 0.05$, **$P \leq 0.01$, ***$P \leq 0.001$, ****$P \leq 0.0001$; *n* = 12 (b), 9 (d) embryos, 46 (e and f, control;), 52 (e and f, durotaxis), 50 (e and f, chemotaxis), 56 (e and f, both), 44 (e and f, *in vivo*), 22 (g, control), 33 (g, durotaxis), 20 (g, chemotaxis), 14 (g, both), 96 (h) clusters. Statistics and reproducibility are in the source data and Methods.

Methods

Xenopus embryos

Xenopus laevis embryos were obtained as previously described[17]. Briefly, ovulation of mature 2-5-year-old females was induced by injecting 100 IU pregnant mare serum gonadotrophin (Intervet) subcutaneously into the dorsal lymph sac. 72 hours later, a second injection of 200-300 IU human chorionic gonadotrophin (Intervet) was performed. Eggs were fertilised *in vitro* by mixing with a sperm solution. Testes were provided by the European Xenopus Resource Centre. Embryos were staged according to Nieuwkoop and Faber[28]. Fertilised eggs were de-jellied in a solution of 1 g L-cysteine (Sigma-Aldrich) and 500 μl 5 N NaOH in 50 ml H_2O and maintained in 0.1x MMR or 3/8 normal amphibian media (NAM). Animal licenses were approved by the Animal Welfare and Ethical Review Board (WERB) at University College London and the UK Home Office. All animal experiments followed the relevant guidelines and regulations.

Embryo micromanipulation

Neural crest or placodes were dissected as previously described[12]. In brief, using a hair knife, the overlying ectoderm was lifted, and the neural crest or cranial placode removed. Dissection was performed in 3/8 NAM. Grafting was also performed similar to previously described[17]. Briefly, neural crest was removed and transplanted to the region immediately ventral to the cranial placodes. The overlying ectoderm was unfolded back on top, and a glass coverslip placed on top until the embryo fully healed, after which the coverslip was removed.

Stiffness gradient ablation was achieved by making a mechanical cut with a hair knife anterior and dorsal and away from the neural crest, close to the midline, similar to previously described[11], and illustrated diagrammatically in Fig. 2a. In bead experiments, heparin-acrylic beads (Sigma H263, Adar Biotech 6024-1) were incubated with 1 μg/mL Sdf1 solution. A small cut into the ectoderm was made using a hair knife, which was also used to rid the adhesion of the ectoderm from the underlying tissues. The bead was inserted with forceps under the ectoderm. Beads were placed either into a position along the normal presumptive neural crest path or dorsal (the opposite direction). Only embryos that fully healed were analysed. For

exogeneous pressure experiments, the tip of a glass microneedle was cut and placed on an appropriate region of the embryo (depending on the experiment) without damaging the embryo. The rounded needle was held in place by a micromanipulator for 5 h.

mRNA synthesis, morpholinos, microinjection and reagents

mRNA templates were generated as previously described[17]. In brief, mRNA was transcribed with mMESSAGE mMACHINE SP6 transcription Kit (Thermo-Fisher AM1340). Sdf1 and Twist morpholinos were synthesised by GeneTools (GeneTools) and used as previously described[17,19,29]. *Xenopus* embryo microinjections were performed as previously described[17]. Embryos were microinjected with a 5 nl solution into two blastomeres (one dorsal blastomere and one ventral blastomere, on one side of the embryo) at the eight-cell stage using a calibrated needle. LifeAct-Ruby, MLC-GFP, nuclear RFP, membrane GFP, Sdf1 morpholino and Twist morpholino were injected as previously described[12,17,19,29].

Polyacrylamide hydrogels

Glass slides and glass coverslips were prepared as previously described[11]. In brief, glass slides were coated in a solution containing 14-parts ethanol, 1-part acetic acid and 1-part PlusONE Bind-Silene (GE Healthcare). Slides were washed in ethanol and air dried. Glass coverslips were coated for 15 min with PlusONE Repel-Silene (GE Healthcare) and air dried. Preparation of polyacrylamide gels was guided by the extremely useful table of gel preparation solutions outlined by Tse and Engler[30]. For shallow gradient gels, two polyacrylamide solutions were prepared. For soft gels, a mix containing 550 µl 7.6 mM HCl, 396.5 µl H2O, 0.5 µl TEMED, 60 µl 40% acrylamide and 20 µl bis-acrylamide was prepared. For stiff gels, a mix containing 550 µl 7.6 mM HCl, 396.5 µl H2O, 0.5 µl TEMED, 60 µl 40% acrylamide and 20 µl bis-acrylamide was prepared. 6 µl 0.2 µm carboxylate-modified fluorophores were added to the stiff gel for observation of a gradient in beads upon successful gradient formation.

Bind-Silene-coated glass slides were placed on top of an uncoated glass slide. Two 1-mm thick U-shaped PDMS shapes were placed on top of the coated glass slide, with their edges hanging off the edge of the slide. Repel-Silene-coated glass

coverslip were placed on the PDMS, and then a third uncoated glass slide was placed on top. The stack was sandwiched by clips and angled at 45°.

Polymerisation of the soft and stiff solutions was started by adding 5 ml 10% ammonium persulphate (GE Healthcare) to each mix. The stiff gel solution was added between the glass coverslip and the PDMS by a 20 μl pipette up to halfway. One minute later, the soft gel solution was added. For uniform gels, only the soft gel solution was added. Polymerisation proceeded for 15 min, before the sandwich was disassembled, and the coverslip removed. Gels were washed three times for 5 mins with 10 mM HEPES.

Fibronectin was covalently crosslinked to gels via Sulfo-SANPAH-mediated succinimide crosslinking, as previously described[11]. Briefly, gels were twice incubated in 50 ng/μl Sulfo-SANPAH (Thermo-Fisher 22589) in the presence of UV light and washed with 10 mM HEPES. Gels were incubated with 10 mg/ml fibronectin overnight and washed with 10 mM HEPES. Effective Young's modulus for each gel was determined by nanoindentation and functionalisation was checked by immunostaining against fibronectin (DSHB, 4H2) (Fig. 1b; Extended Data Fig. 1d, f, h; Extended Data Fig. 2a).

Nanoindentation

Stiffness measurements were performed using nanoindentation (Chiaro, Optics11Life, Piuma V2 Version 3.4.3), as previously described[31-34]. Cantilevers were customised by Optics11 Life. Probes had a spherical glass tip ~20 μm in radius mounted on an individually calibrated cantilever with a spring constant of ~ 0.025 N m^{-1}. Deformation of the cantilever following contact with the sample (polyacrylamide gel or embryo) was measured by tracking the phase-shift in light, reflected from the back of the cantilever. Samples were indented to a depth of 2 μm with a velocity of 2.5 μm s^{-1}. The tip was held in this indentation depth for 1 s, and retracted over 1 s. The Young's moduli were calculated automatically by the software, by fitting the force versus indentation curve to the linear Hertzian contact equation model[32]. The effective Young's modulus (E), referred to in this manuscript as apparent elasticity (App. elasticity), is derived from the fit of the loading force-displacement curve ($F(h)$), the indenter tip radius (R), and the indentation depth (h), according to the following

formula, for which a Poisson's ratio (v) 0.5 was assumed, and was calculated automatically by the software (Chiaro, Optics11Life, Piuma V2 Version 3.4.3).

$$F = \frac{4}{3} K \sqrt{r} \delta^{\frac{3}{2}} = \frac{4}{3} \frac{E}{1 - v^2} \sqrt{r} \delta^{\frac{3}{2}}$$

Embryos were prepared for nanoindentation as previously described. Briefly, a small hole was carved into a clay modelling dish and the embryo mounted inside to ensure it did not move during measurements. Embryos were maintained in 3/8 NAM. The epidermis was carefully lifted using a hair knife[36,37]; the epidermis does not contribute to the effective Young's Modulus of the placodes (Extended Data Fig. 2f) or the mesoderm[11]. Nanoindentations were performed in the region immediately ventral to the neural crest as shown by the boxes in Fig. 1c. For gels to be measured, they were incubated in DFA media, which is the same media used for culture of neural crest cells. All embryo and gel measurements were performed and analysed independently by both authors. Nanoindentation data were analysed with Optics11 Data Viewer V2.4.0.

Neural crest culture

Neural crest was cultured as previously described[17]. For chemotaxis experiments, heparin-acrylic beads were incubated with 100 ng/ml Sdf1 overnight, and then placed on the gel in the same direction as the stiffness gradient where appropriate. Culture of placodes was also performed a previously described[12]. Recombinant N-Cadherin was used at 3 μg/ml as previously described[12].

Time-lapse microscopy and laser ablation

Time-lapse imaging and laser ablation were performed as previously described[17]. Imaging of neural crest explants overnight was performed on a compound microscope (Nikon Eclipse 80i; Simple PCI Version 6.6, and DM5500, Leica; LAS AF Version 2.6.0.7266) or on a confocal microscope (SP8vis, Leica; Las X Version 3.5.19976). Actin and myosin imaging in explants, and neural crest graft imaging was performed on a confocal microscope (SP8vis, Leica; Las X Version 3.5.19976).

100% power of a 740 nm laser of a LSM880 Multiphoton microscope (Zen Blue Version 14.0.0.201) was used for photoablation. The 740 nm laser line was for photoablation was achieved using the microscope's Ti:Sapphire laser tuneable

between wavelengths 720-1064 nm. Ablations were repeated as necessary upon reformation of the actomyosin cable, as previously described, at a rate of approximately one ablation per minute[17]. Ablations were performed on small, manually defined region of interest on a single *z*-plane. Average laser power at the objective lens was 600 mW.

Analysis of neural crest migration and actomyosin contraction

Analysis of neural crest migration was performed as previously described[17,37]. Briefly, the ImageJ plugin, Manual Tracking, was used to track cells or clusters and Chemotaxis Tool (Ibidi) used to quantify tactic index or speed. The formula used for the tactic index within the Chemotaxis Tool plugin is simplified in Extended Data Fig. 4l, with full formula for calculation found on the Ibidi website (https://ibidi.com/chemotaxis-analysis/171-chemotaxis-and-migration-tool.html). Angles were calculated either manually or through the Chemotaxis Tool. Colour-coded temporal projections were made on ImageJ using Temporal-Color Code. Percentage of explants undergoing directional migration (Fig. 9i) was calculated based on the degree of movement along the gradient; strong is classified as movement of more than the diameter of the cluster in the direction of the gradient; moderate is classified as between half and one diameter movement of the cluster in the direction of the gradient over 6 h. Ectopic migration index was calculated as defined in Extended Data Fig. 7e, f.

Actomyosin length calculations, front movement relative to rear contraction, and angles of contraction were performed as previously described[17]. Briefly, the ImageJ line tool was used to measure actomyosin length. The line tool was also used to measure fibronectin thickness. Heat maps were by GraphPad Prism8. Angles were measured manually using ImageJ and rose plots generated using Oriana 4.01 or the Chemotaxis Tool plugin (Ibidi). Blebbistatin (abcam, ab12042) was used as previously described[17]. The kymograph in Fig. 6b was made using the KymoResliceWide plugin on ImageJ. The kymograph was partially manually reconstructed from lines of multiple manually made kymographs to account for cell movement in the XY.

***In situ* hybridisation and immunostaining**

Colorimetric whole mount *in situ* hybridisation was performed as previously described[37]. Briefly, *Twist*-digoxigenin riboprobe was transcribed with a Riboprobe *in* vitro Transcription System (Promega P1420). Embryos were fixed in MEMFA, bleached in 6% hydrogen peroxide, and then incubated with probes for Twist, Eya1 and/or Foxi1c overnight in hybridisation buffer (Eya1 and Foxi1c probes were kindly gifted by E. Theveneau). Embryos were then washed, blocked with 2% blocking reagent, incubated with 1:3000 anti-digoxigenin-AP antibody, and then revealed with NBT/BCIP with AP buffer. Embryos were imaged using a Nikon SMZ800N attached to a DS-Fi3 camera (Nikon DS-L4 Version 1.4.0.4).

Fluorescent *in situ* hybridisation was performed similar to previously described[35]. In brief, embryos were fixed in MEMFA and incubated with Twist probe overnight in hybridisation buffer. Embryos were washed, bleached in 3% hydrogen peroxide, incubated with 1:1000 anti-digoxigenin-POD antibody. After washing, embryos underwent the fluorescent POD reaction with Cy3-tyramide solution. For subsequent immunostaining, embryos were embedded in a 15% sucrose/30% fish gelatin solution, frozen on dry ice and cryosectioned into 30 μm slices. Slides were incubated at 37°C for 1 h and then at RT overnight, washed with PBS, blocked in 10% NGS, and then incubated in anti-fibronectin antibody (1:60; DSHB; 4H2), anti-Sox3 antibody (1:200; kindly gifted by M. Klymkowski)[29,39-41], and then AlexaFluor secondary antibody (1:350) and DAPI (1:1000). Sections were mounted and imaged on a Leica SP8 confocal microscope. Images were stitched were appropriate using the Pairwise Stitching plugin on FIJI v1.53k.

For immunostaining of neural crest and placodes *ex vivo*, explants were fixed in 4% formaldehyde, blocked in 10% NGS and then incubated in anti-active Rac-GTP antibody (1:500, NewEast Biosciences, 26903)[42], anti-vinculin antibody (1:500, Sigma, V9131)[43] or Alexa-conjugated Phalloidin (1:500, Thermo Fisher, A34055) and then AlexaFluor secondary antibody (1:350, Thermo Fisher) and DAPI (1:1000, Sigma, D9542) where appropriate.

Xenopus **diagrams**

Several diagrams are adapted from *Normal table of Xenopus laevis (Daudin)*. Copyright © 1994, Nieuwkoop and Faber[28]. Reproduced by permission of Taylor and

Francis books US. Digital images created by Xenbase (http://www.xenbase.org/, RRID:SCR_003280)[44].

Statistics and Reproducibility

Normality in the spread of data for each experiment was tested using the Kolmogorov-Smirnov, d'Agostino-Pearson and Shapiro-Wilk tests in Prism8 (GraphPad). Significances for datasets displaying normal distributions were calculated in Prism8 with an unpaired two-tailed Student's *t*-test or one-way analysis of variance (ANOVA) with post-hoc Tukey's test for multiple comparisons. Significances for non-normal distributed data were calculated in Prism8 with a two-tailed Mann-Whitney *U* test, Wilcoxon match-pairs signed rank test or Kruskal-Wallis test with host-hoc Dunn's test for multiple comparisons. Apart from the following, all experiments were performed 3 times; Fig. 1e $N = 4$, Fig. 1g, c $N = 4$, Fig. 1l-n $N = 5$, Fig. 4c, d and Extended Data Fig. 7e-l $N = 5$, where N refers to the number of experimental replicates, with biologically independent experiments.

All stars of statistical significance or lack or significance (ns) refer to comparison to the control, unless otherwise indicates comparison to the control.

Authors were not blinded to embryos or cells. Criteria for selection was survival and correct delivery of the injected treatments. Embryos and cells were allocated into experimental groups randomly. No predetermination of sample sizes was done. Stated in the Statistics and Reproducibility section of the methods.

Statistical tests for synergy effects between durotaxis and chemotaxis were performed using a resampling paradigm. For each test, possible experimental outcomes under the null hypothesis were simulated by stochastic sampling from existing data. Specifically, data from the durotaxis-only and chemotaxis-only conditions (and, where appropriate, from control) were resampled and combined to represent an additive (non-synergistic) null hypothesis. *P*-values were then determined by checking how frequently the resampled outcome performs as well or better with respect to a given test statistic compared to the experimental condition where both durotactic and chemotactic cues were present (i.e., the putatively synergistic condition). For synergy statistics, tests used are one-tailed.

To test for synergy of speed (Extended Data Fig. 9k), resampling was performed on control, durotaxis-only and chemotaxis-only conditions. The differences of the durotactic and chemotactic conditions to the control were summed and added to the control, resulting in a hypothetical speed under an additive null model. To determine the *P*-value, the mean of these additive speeds across 30 random samples was then compared to the mean of the durotaxis plus chemotaxis experimental condition, across a total of 10^6 resampling experiments. To test for synergy of tactic index, directionality, and migration distance (Extended Data Fig. 9j, l, m), full tracks of cluster migration were stochastically simulated by sampling from durotaxis-only and chemotaxis-only motion vectors and performing vector addition to represent the additive null hypothesis. Resampled vectors were accumulated over 30 time points to generate tracks. For each simulated experiment (10^5 in total), 30 sample tracks of 30 time points each were generated. Measurements were extracted from the resulting tracks and compared to the durotaxis plus chemotaxis experimental data.

For Fig. 1, heat maps (c) are from representative embryos, heat maps (d-f, h, m) and thick bars (i, k, n) represent mean; error bars (i, k, n) represent s.d.; unpaired two-tailed *t* test (i, k), Dunn's test (n); ns, $P>0.05$, $^{**}P\leq0.01$, $^{****}P\leq0.0001$; $n = 8$ (d), 10 (e; n, Ctrl, MO-NCad + Push), 22 (MO-NCad) embryos, 16 (i, k) explants.

Data availability

The data that support the findings of this study are available within the Article and its Supplementary Information. Source data for Figs. 1-4 and Extended Data Figs. 1-10 are provided with the paper.

28 Nieuwkoop, P. & Faber, J. *Normal table of Xenopus laevis (Daudin) : a systematical and chronological survey of the development from the fertilized egg till the end of metamorphosis*. 2nd edn edn, (North-Holland, 1967).
29 Shi, J. L., Severson, C., Yang, J. X., Wedlich, D. & Klymkowsky, M. W. Snail2 controls mesodermal BMP/Wnt induction of neural crest. *Development* **138**, 3135-3145, doi:10.1242/dev.064394 (2011).
30 Tse, J. R. & Engler, A. J. in *Current Protocols in Cell Biology* Vol. 47 (Wiley Interscience, 2010).
31 Yue, L., Wang, S., Wulf, V. & Willner, I. Stiffness-switchable DNA-based constitutional dynamic network hydrogels for self-healing and matrix-guided controlled chemical processes. *Nature Communications* **10**, doi:10.1038/s41467-019-12697-2 (2019).
32 Giobbe, G. G. *et al.* Extracellular matrix hydrogel derived from decellularized tissues enables endodermal organoid culture. *Nature Communications* **10**, doi:10.1038/s41467-019-13605-4 (2019).
33 Karoutas, A. *et al.* The NSL complex maintains nuclear architecture stability via lamin A/C acetylation. *Nature Cell Biology* **21**, 1248-+, doi:10.1038/s41556-019-0397-z (2019).
34 Chen, C. Y. *et al.* Suppression of detyrosinated microtubules improves cardiomyocyte function in human heart failure. *Nature Medicine* **24**, 1225-+, doi:10.1038/s41591-018-0046-2 (2018).
35 Ding, Y., Xu, G. K. & Wang, G. F. On the determination of elastic moduli of cells by AFM based indentation. *Scientific Reports* **7**, doi:10.1038/srep45575 (2017).
36 Gouignard, N., ChristianTheveneau, Eric. in *The Epithelial-to Mesenchymal Transition* Vol. 2179 *Methods in Molecular Biology* (ed Theveneau E. Campbell K.) 257-274 (2021).
37 Barriga, E. H., Shellard, A. & Mayor, R. in *Neural Crest Cells* Vol. 1976 *Methods in Molecular Biology* (ed Sophie Wiszniak Quenten Schwarz) 135-152 (Humana Press, 2019).
38 Dubaissi, E. *et al.* A secretory cell type develops alongside multiciliated cells, ionocytes and goblet cells, and provides a protective, anti-infective function in the frog embryonic mucociliary epidermis. *Development* **141**, 1514-1525, doi:10.1242/dev.102426 (2014).
39 Zhang, C., Basta, T., Jensen, E. D. & Klymkowsky, M. W. The beta-catenin/VegT-regulated early zygotic gene Xnr5 is a direct target of SOX3 regulation. *Development* **130**, 5609-5624, doi:10.1242/dev.00798 (2003).
40 Schlosser, G. & Ahrens, K. Molecular anatomy of placode development in Xenopus laevis. *Developmental Biology* **271**, 439-466, doi:10.1016/j.ydbio.2004.04.013 (2004).
41 Schlosser, G. *et al.* Eya1 and Six 1 promote neurogenesis in the cranial placodes in a SoxB1-dependent fashion. *Developmental Biology* **320**, 199-214, doi:10.1016/j.ydbio.2008.05.523 (2008).
42 Cao, X. *et al.* A phosphorylation switch controls the spatiotemporal activation of Rho GTPases in directional cell migration. *Nature Communications* **6**, doi:10.1038/ncomms8721 (2015).
43 Kanoldt, V. *et al.* Metavinculin modulates force transduction in cell adhesion sites. *Nature Communications* **11**, doi:10.1038/s41467-020-20125-z (2020).
44 Karimi, K. *et al.* Xenbase: a genomic, epigenomic and transcriptomic model organism database. *Nucleic Acids Research* **46**, D861-D868, doi:10.1093/nar/gkx936 (2018).

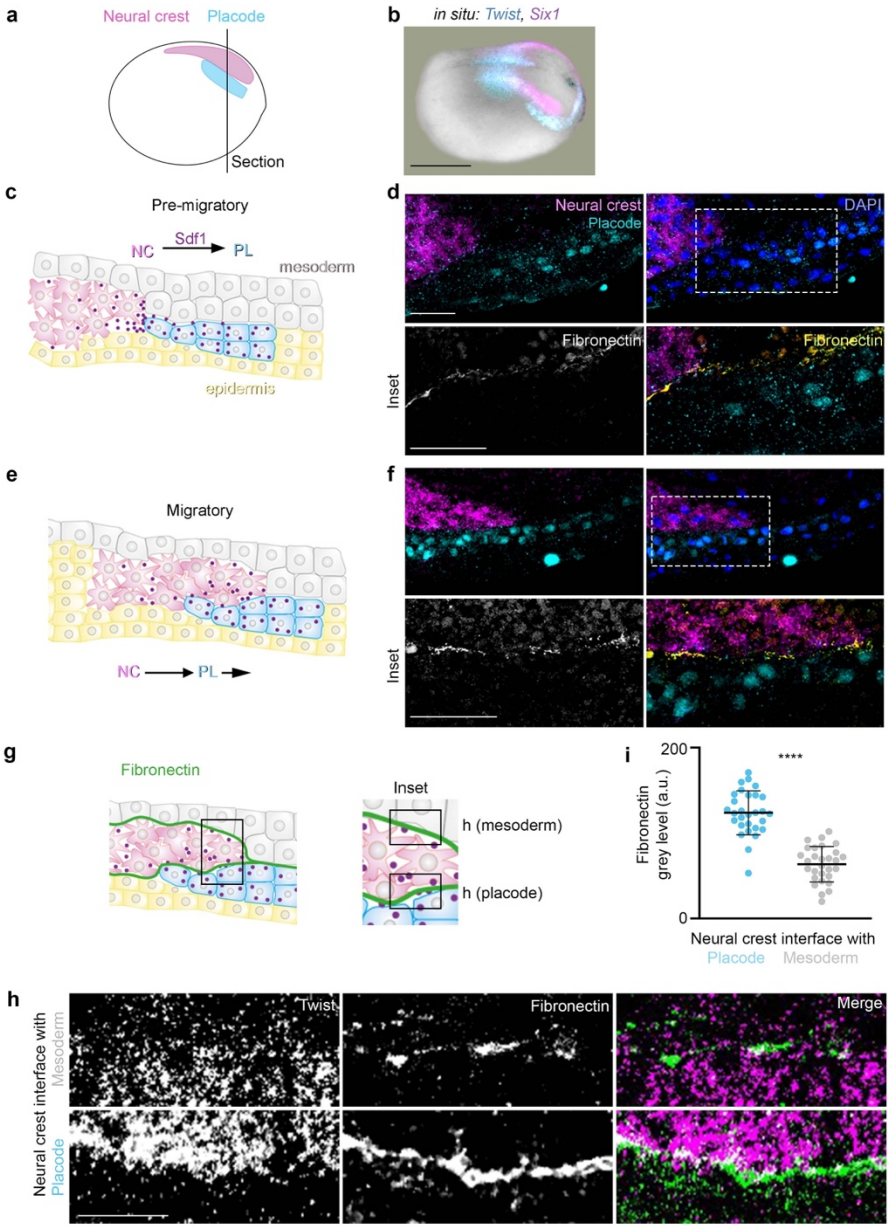

Extended Data Figure 1. Neural crest use Placodes as substrate for migration. a, Schematic of lateral view of an embryo showing the position of neural crest (pink) and placodes (blue) before neural crest migration. The black line represents the position of a cross section shown in c. **b,** Double *in situ* hybridisation against the placodal marker *Six1* and the neural crest marker *Twist* at pre-migratory stage[23] Scale bar is 500 µm (b). **c, e,** Diagram illustrations of the neural crest environment *in vivo*, engaged in "chase and run"[12] interaction with placodes. The diagram is illustrative of a cross-section through the embryo, has illustrated by the black line in a. Neural crest (pink) chemotax toward Sdf1-secreting placode (Sdf1, purple; placode, blue). The two cell types interact causing placode to run away. **d, f,** Cryosection images showing fluorescent *in situ* hybridisation for Twist (neural crest, magenta), and immunostaining for Sox3 (placodes, cyan) and fibronectin (grey in single channel; yellow in merge). The fibronectin and merge panels are zooms of the white dashed boxes. Note that the neural crest migrates toward the placodes and that a fibronectin layer interfaces the two tissues. Scale bar is 50 µm (d, f). **g, i,** Fibronectin surround neural crest stream. **g,** Schematic of fibronectin (green) surrounding the neural crest at the interface with mesoderm and placodes. **h**, Double ISH (Twist) and immunostaining (fibronectin) at the interfaces shown in

the squares in g. Scale bar is 20 µm (h) **i,** Quantification of fibronectin levels at the interface of neural crest with Placodes and Mesoderm. Note the higher levels of fibronectin at the interface of neural crest and placodes than with mesoderm. Thick bars (i) represent mean; error bars (i) represent s.d.; unpaired two-tailed *t*-test (i); ****$P \leq 0.0001$; $n = 29$ embryos each (i). Statistics and reproducibility are in the source data and Methods.

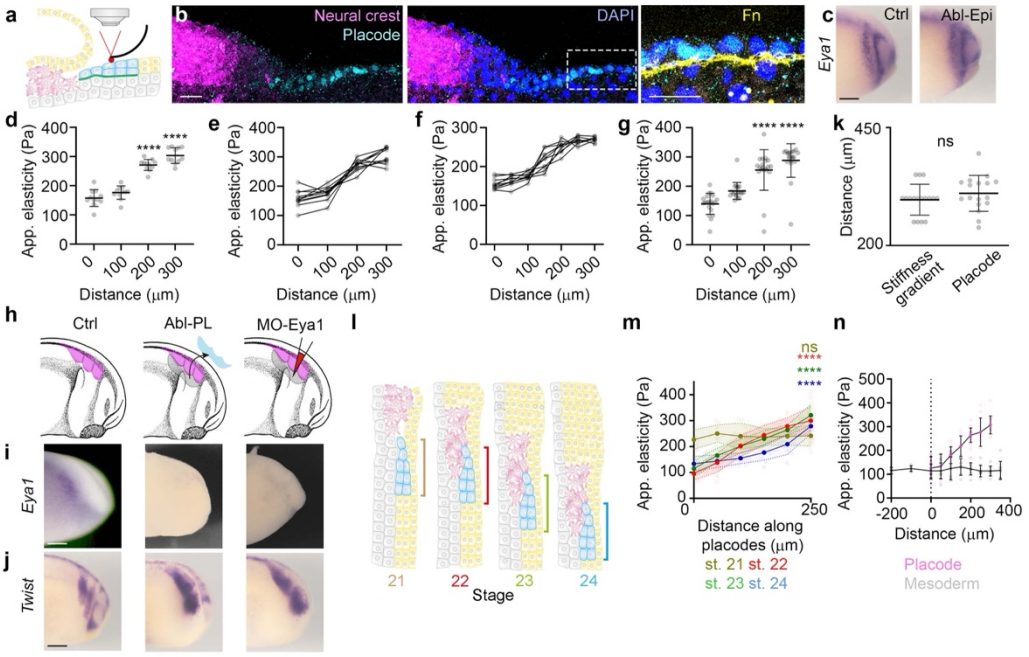

Extended Data Figure 2. Dynamic stiffness gradient in placode cells. a-b, Diagram illustrating removal of the epidermis to expose the placodes for atomic force microscopy (a). Cryosection images (b) showing that the placodes are the most superficial tissue after epidermis removal. The right merge panel is a zoom of the white dashed box. Scale bar is 50 µm (b). **c,** *in situ* hybridisation against the placodal marker *Eya1* at migratory stages on a representative embryo on the control side and side where the epidermis was dissected. Note that the placodal tissue is unaffected by epidermal dissection. Scale bar is 200 µm (c). **d-g,** Apparent elasticity measurements *in vivo* at the start of neural crest migration (c, d). Note that b and c represent the same data set. Stiffness measurements of the representative heat map in Fig. 1d, a stage 22 embryo (e) and where the epidermis was not removed (f). **h-j,** Placode deletion. **h,** Schematics of the different treatments. **i**, *in situ* hybridisation against the placodal marker Eya1 after each treatment. Stiffness values after each treatment are shown in Fig 1d. Scale bar is 200 µm (i). **j,** *in situ* hybridisation against the neural crest marker *Twist* in conditions stated. Note that neural crest migration depends on cranial placodes. Scale bar is 200 µm (j). **k**, Quantification of the distance of stiffness gradients measured by nanoindentation and cranial placode tissue *in vivo*. **l-n**, Diagram illustration of the neural crest and placodes *in vivo* (l). The area indicated represent the placode whose stiffness was measured after epidermis removal (not shown). Quantification of apparent elasticity measurements of the cranial placodes (m). Note that the gradient emerges at the onset of neural crest migration, and that the gradient persists as the neural crest migrate over time. A corresponding heat map representing averaged stiffness for embryos at different stages along the dorsoventral axis is sown in Fig 1e. Comparison of mesodermal and placodal stiffness over the dorsoventral axis (n). The dashed line indicates the rear of the placode. Thick bars (d, g, k, m, n) and circles (m) represent mean; error bars represent s.d. (d, g, k, m, n); Tukey's test (d), Dunn's test (g), two-tailed Mann-Whitney *U* test (k), Wilcoxon match-pairs signed rank

test (m, st. 21), paired two-tailed *t*-test (m, st. 22, st. 23, st. 24); ns, $P>0.05$, ****$P\leq0.0001$; n = 11 (d, e), 20 (g), 17 (k), 10 (m) embryos, 10 (f) linear lines. Diagrams in **h** are adapted from *Normal table of Xenopus laevis (Daudin): a systematical and chronological survey of the development from the fertilized egg till the end of metamorphosis*. Copyright © 1994, Nieuwkoop and Faber. Reproduced by permission of Taylor and Francis books US. Statistics and reproducibility are in the source data and Methods.

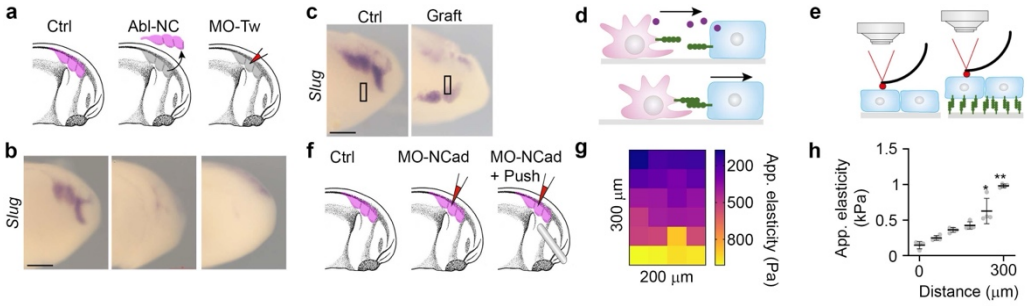

Extended Data Figure 3. The neural crest self-generates the stiffness gradient through N-Cadherin. a, b, Schematics indicating the different treatments (a) and embryos stained by *in situ* hybridisation for the neural crest marker, *Slug* (b). Heat maps of this experiments are shown in Fig. 1f. Scale bar is 200 µm (b). **c,** Embryos stained by *in situ* hybridisation for the neural crest marker, *Slug*. Black boxes represent the region in which nanoindentation was performed; mean stiffness heat map of each condition is shown in Fig. 1h. Scale bar is 200 µm (c). **d**, Diagram illustrating "chase and run"[12]. Neural crest (pink) chemotax toward Sdf1-secreting placode (Sdf1, purple; placode, blue). The two cell types interact through N-Cadherin (green), causing placode to run away (migration indicated by black arrow). **e**, Diagram illustrating placode cultured on fibronectin (grey) or fibronectin with N-Cadherin. Placodal stiffness measured in these conditions is shown in Fig. 1i. **f**, Schematics indicating the different treatments. Results are shown in Fig. 1l-n. **g, h,** exogenous stiffness gradient formation. Stiffness heat map from a representative embryo in which an exogeneous local pressure was applied ventral to the neural crest as depicted in g (bottom of the heat map, g), and quantification along the axis (h). Thick lines (h) represent mean; error bars (h) represent s.d.; Dunn's test (h); *$P\leq0.05$, **$P\leq0.01$; n = 4 (h) linear lines. Diagrams in **a, f** are adapted from *Normal table of Xenopus laevis (Daudin)*. Copyright © 1994, Nieuwkoop and Faber. Reproduced by permission of Taylor and Francis books US. Statistics and reproducibility are in the source data and Methods.

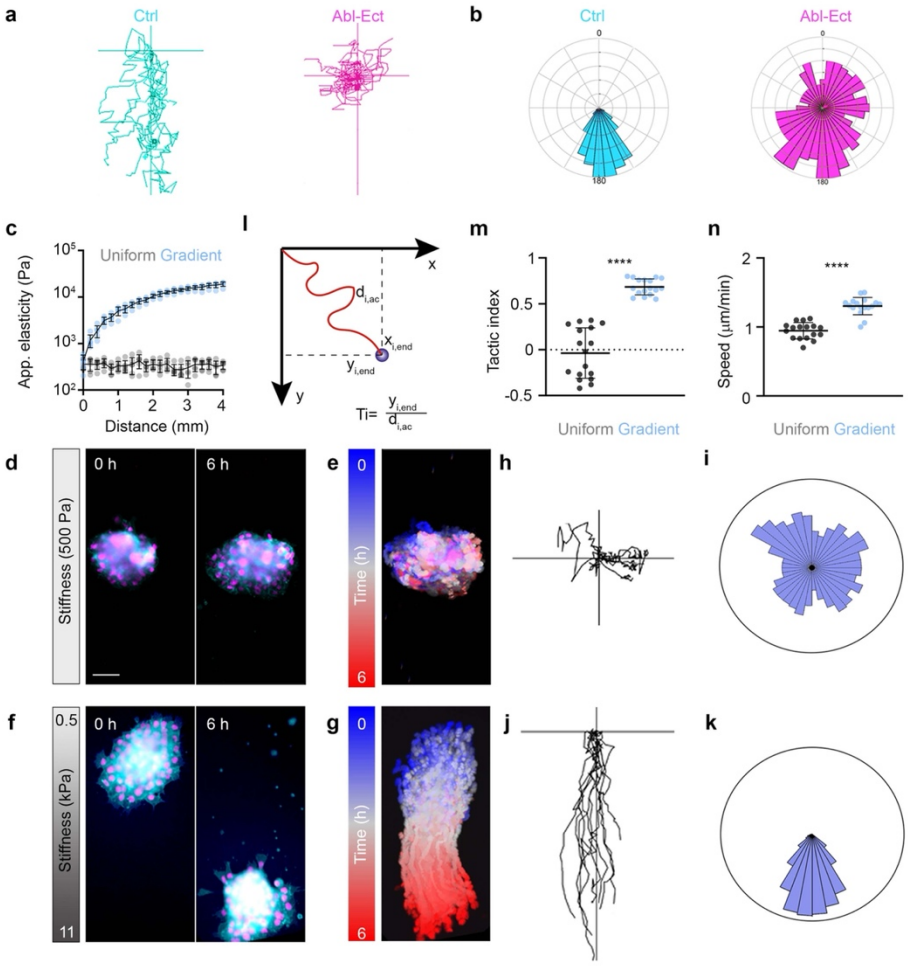

Extended Data Figure 4. Neural crest durotaxis *in vivo* and on steep gradients *ex vivo*. **a, b**, Graft of fluorescently labelled neural crest into control embryos (cyan) or ablated embryos (magenta; **a**, centred cell tracks; **b**, track angles). Grafted embryos are shown in Fig. 2d, e. **c**, Apparent elasticity measurements of steep stiffness (blue) and uniform (grey) gradient gels. **d-g**, Neural crest explants with labelled nuclei (magenta) and membrane (cyan) (d, f) and time-coded projected tracks (e, g) on gels of uniform stiffness (d, e) and graded stiffness (f, g). Scale bar is 50 µm (d-g). **h-k**, Cell tracks (h, j) and angles of movement (i, k) from clusters on gels of uniform (h, i) or graded (j, k) stiffness; **l-n**, Formula for tactic index (l), quantification of tactic index (m) and speed (n). Thick bars (c, m, n) represent mean; error bars (c, m, n) represent s.d.; two-tailed Mann-Whitney *U* test (m, n); ****$P \leq 0.0001$; $n = 6$ (c) gels, 360 (i, k) cells from 18 clusters, 17 (m, n) explants. Statistics and reproducibility are in the source data and Methods.

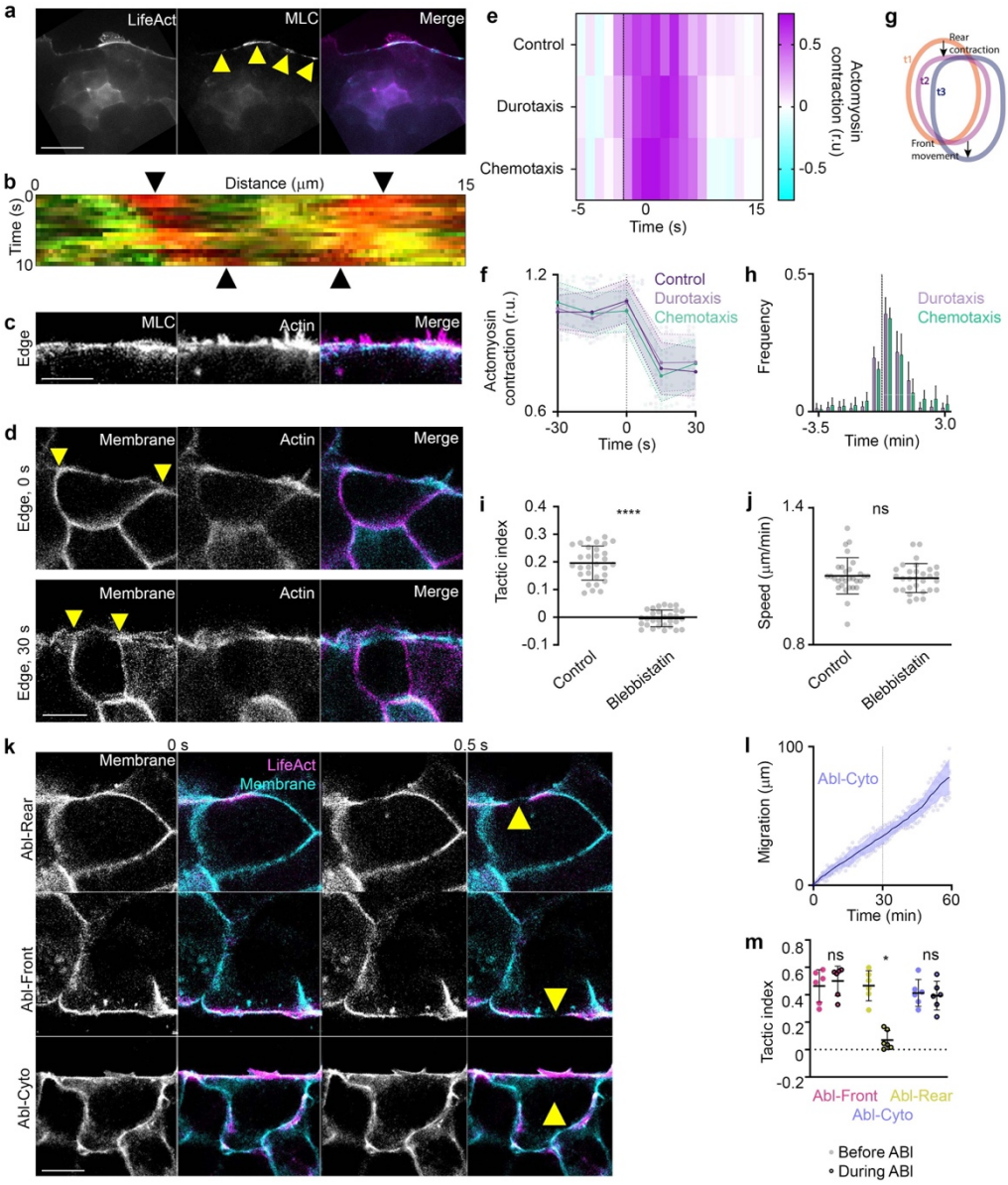

Extended Data Figure 5. Rear actomyosin contraction is essential for collective durotaxis. a, Neural crest *in vivo* expressing fluorescently tagged myosin light chain II (MLC) and LifeAct. Note that a supracellular actomyosin cable exists at the edge of the neural crest cell group *in vivo*. Arrowheads indicate the actomyosin cable. Scale bar is 25 μm (a). **b**, Kymograph of the edge of the neural crest cluster *in vivo*. Green represents MLC, which is absent from cell-cell contacts, and red represents LifeAct. Note the *in vivo* contraction of the actomyosin cable. Cell-cell contact contraction is indicated with the black arrowheads. **c,** Neural crest *ex vivo* expressing fluorescently tagged myosin (MLC, myosin light chain), LifeAct and membrane marker. Corresponding low magnifications are shown in Fig.4a. Scale bar is 25 μm (c). **d,** Two time points from the edge of a neural crest cluster on a stiffness gradient. Yellow arrowheads mark cell-cell contacts. Note the contraction of the actomyosin cable and reduction in length between cell contacts. Scale bar is 10 μm (d). **e**, Heat map of an example actomyosin contraction at the edge of clusters in control, durotaxis and chemotaxis. Time point zero represents the start of actomyosin contraction. **f,** Quantification of actomyosin contraction by cable length. Note that the amplitude of contraction is the same in all conditions. **g, h**, An illustrative diagram showing rear contraction and front movement of a cluster (circle outline) at three time points (g), and a histogram representing the time at which front movement occurs

relative to rear contraction (h). The dashed line indicates the rear contraction time point reference, t = 0. **i, j,** Tactic index (i) and speed (j) of clusters on shallow stiffness gradient gels exposed to the myosin II inhibitor, blebbistatin. **k-m,** Pictures of membrane and merge of LifeAct and membrane for the example ablation shown in Fig. 3c-g (k, top, middle) or for cytoplasmic ablation (k, bottom). Yellow arrowheads indicate location of ablation. Scale bar is 10 μm (k). **l**, Migration of neural crest clusters on physiological stiffness gradients. The dashed line (start of ablations) separates before and during laser ablation of the cytoplasm. **m,** Tactic index of clusters before and during actomyosin cable ablation in the front or rear portion of migrating cell groups, or in the cytoplasm. Thick bars (f, i, j, l, m) represent mean; error bars (f, i, j, l, m) represent s.d.; unpaired two-tailed *t*-test (i), two-tailed Mann-Whitney *U* test (j), Dunn's test (m); ns, $P>0.05$, *$P\leq0.05$, ****$P\leq0.0001$; $n = 20$ (f), 15 (h), 30 (i, j), 6 (l, m) clusters. Statistics and reproducibility are in the source data and Methods.

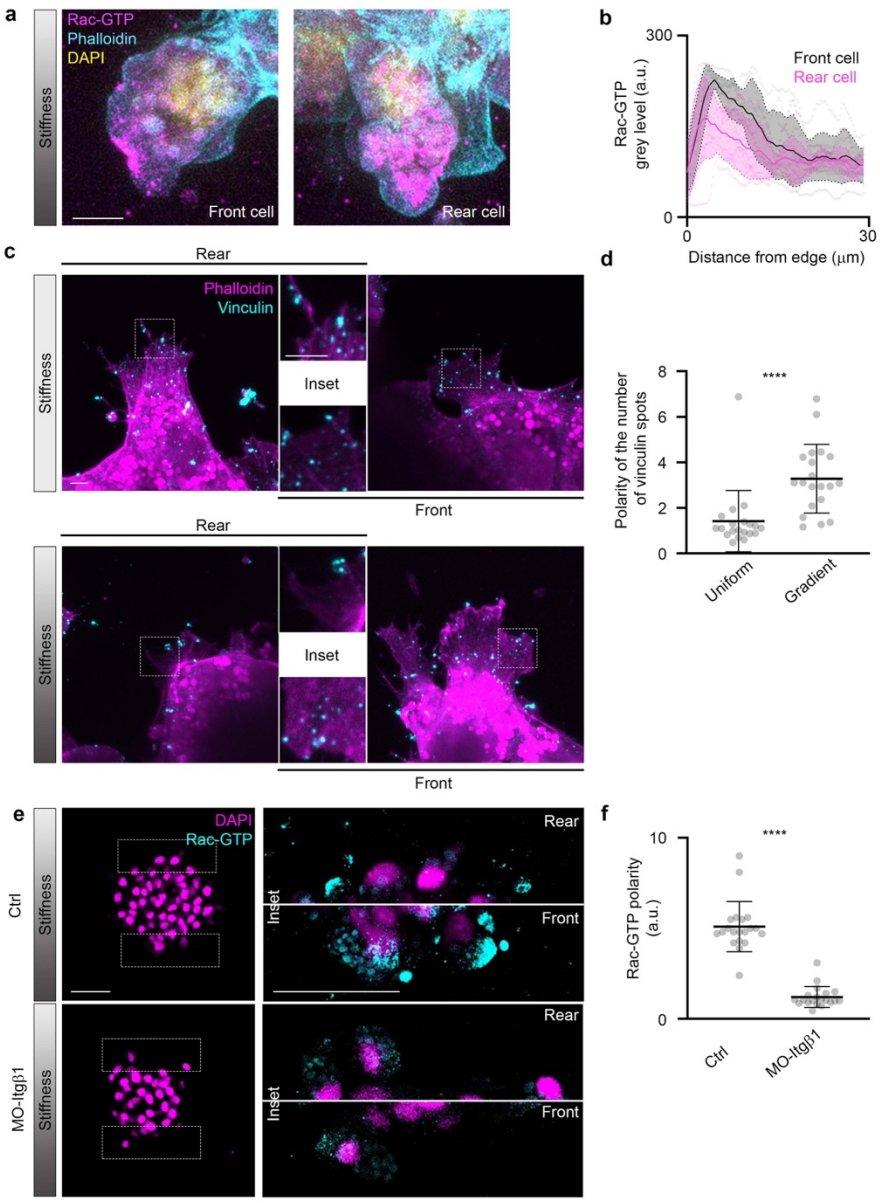

Extended Data Figure 6. Rac during durotaxis. a-b, Cells at the front and rear of neural crest explants on a stiffness gradient, with Rac-GTP, Phalloidin and DAPI labelling (a), and quantification of Rac-GTP along the axis from the edge of the cluster inwards (b). Note that

Rac-GTP preferentially accumulates at the cell edge irrespective of its position within the cluster, consistent with previous observations of Rac polarity. Scale bar is 10 μm (a). **c, d**, Immunostaining of vinculin with Phalloidin in explants on uniform stiffness (c, top; m) or a physiological stiffness gradient (c, bottom) and polarity of the number of vinculin spots quantified (d). Scale bar is 5 μm (c). **e, f**, Immunostaining of Rac-GTP in control or Integrin-β1 knockdown (e) and quantification of its polarity (f). Scale bar is 50 μm (e). Thick bars (b, d, f) represent mean; error bars (b, d, f) represent s.d.; two-tailed Mann-Whitney *U* test (d, f), ****$P \leq 0.0001$; $n = 20$ (b, d, f) clusters. Statistics and reproducibility are in the source data and Methods.

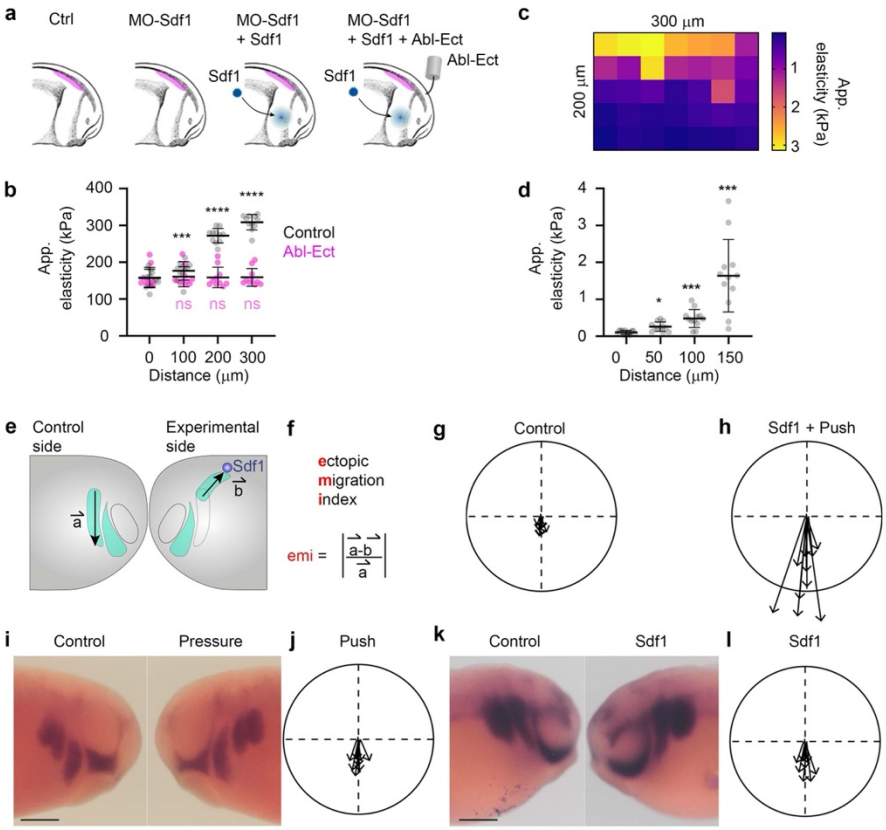

Extended Data Figure 7. Durotaxis and chemotaxis cooperatively coordinate neural crest migration *in vivo*. a, Schematics indicating the different treatments. Results are shown in Fig. 4a, b. **b,** Stiffness measurements in control and ablated embryos. Quantification of *in vivo* migration in each condition is shown in Fig 5b. **c, d,** An example heat map of stiffness from local pressure treatment (c) as depicted in Fig. 4c and quantification of the exogeneous stiffness gradient (d). Results are shown in Fig. 4c. **e-l,** Ectopic migration analysis. **e**, Schematic illustrating how the ectopic migration index (emi) was calculated. For each neural crest stream a vector was drawn from their origin to the final position of migration. The control and experimental side of the same embryos were analysed. For the control side the vector always lays in the migratory pathway, while for the experimental side some vectors point to ectopic locations. **f**, The difference between these two vectors ($\vec{a}$, $\vec{b}$) generates the ectopic migration, which normalized by the control vector corresponds to the **emi**, which is shown as an scalar value in Fig. 4d. **g, h**, emi vectors for the experiment described in Fig. 4c. **i-l**, *In situ* hybridisation for *Twist* of control and experimental side of embryos treated with exogenous local pressure (i, j) or an SDF1 bead (k, l) and the associated vectors. Scale bar is 250 μm (i, k). Thick bars (b, d) represent mean; error bars (b, d) represent s.d.; Tukey's test (b, control; d), Dunn's test (b, ablation); ns, $P > 0.05$, *$P \leq 0.05$, ***$P \leq 0.001$, ****$P \leq 0.0001$; n = 11 (b, control), 10 (b, ablation), 12 (d), 9 (g, h, j, l) embryos. Diagrams in **a** are adapted from *Normal*

table of Xenopus laevis (Daudin). Copyright © 1994, Nieuwkoop and Faber. Reproduced by permission of Taylor and Francis books US. Statistics and reproducibility are in the source data and Methods.

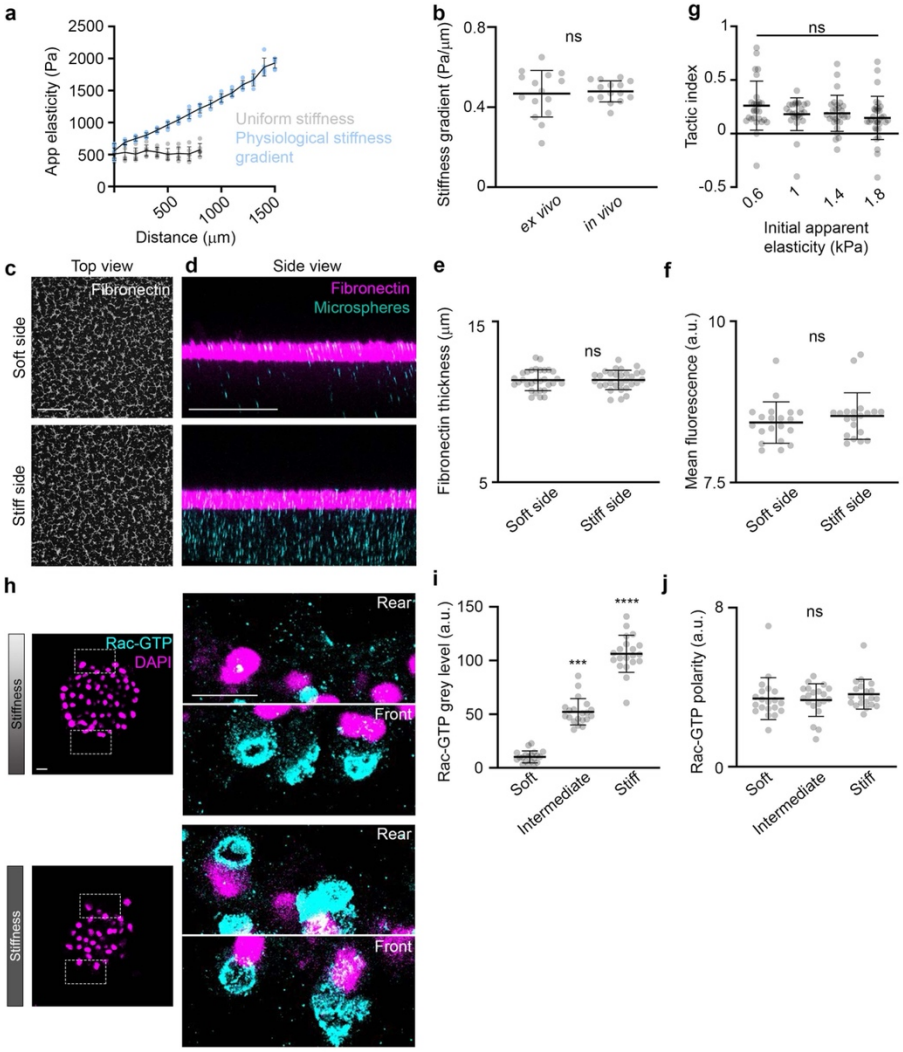

Extended Data Figure 8. Fabrication of physiological stiffness gradient gels. a, Apparent elasticity measurements of shallow (physiological) stiffness gradient gels and uniform stiffness gels. **b**, Gradient of stiffness from *in vivo* embryo measurements and *ex vivo* polyacrylamide gels. **c-d**, Immunostaining of fibronectin and fluorescent microspheres in gel. Images represent soft and stiff sides of the same gel exhibiting a stiffness gradient, in either top view (c) or side view (d). Scale bar is 100 µm (c, d). **e-f**, Quantification of fibronectin thickness (e) and mean fluorescence (f). **g**, Tactic index of clusters seeded on different regions of physiological gradient gels. **h-j**, Immunostaining of Rac-GTP of clusters on a stiffness gradient or uniformly high stiffness (h), quantification of total Rac-GTP (i) and Rac-GTP polarity (j) on different portions of the gradient gel. Scale bar is 20 µm (h). Thick bars (a, b, e-g, i, j) represent mean; error bars (a, b, e-g, i, j) represent s.d.; unpaired two-tailed *t*-test (b, e), two-tailed Mann-Whitney *U* test (f), Dunn's test (g, i, j); *n* = 8 (a), 30 (e), 20 (f), 28 (g, 0.6, 1.4), 25 (g, 1), 33 (g, 1.8) gels, 15 (b) clusters and embryos, 29 (i, j) clusters. Statistics and reproducibility are in the source data and Methods.

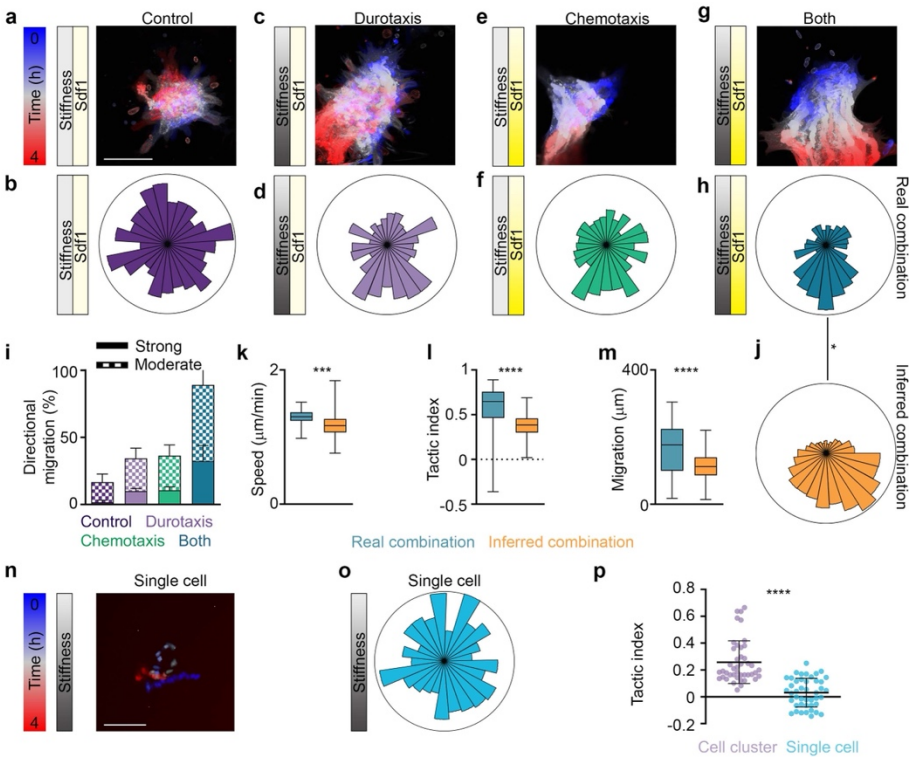

Extended Data Figure 9. Synergistic effects of chemotactic and durotactic gradients and comparison of collective versus single cell durotaxis. a-i, Time-coded projected tracks of example clusters (a, c, e, g), angles of the tracks (b, d, f, h), quantification of directional migration (i). Scale bar is 100 μm (a, c, e, g). **j-m**, Synergy analysis, real combination of chemotaxis and durotaxis is compared with the inferred combination. Clusters exposed to durotactic and chemotactic gradients simultaneously and the inferred addition of track angles (j), speed (k), tactic index (l), and migration distance (m) of clusters exposed to durotactic and chemotactic gradients simultaneously based on the data with either gradient alone. **n**, A time-coded projected track of an individually migrating neural crest cell on a physiological stiffness gradient. Scale bar is 40 μm (n). **o,** A circular histogram showing the angles of the tracks by single cells plated on physiological (shallow) shallow stiffness gradients. **p**, Quantification of tactic index by clusters and single cells on physiological (shallow) stiffness gradients. Box plots (k-m) show the median, box edges represent the 25th and 75th percentiles, and whiskers show spread of data; thick bars (p) represent mean; error bars (p) represent s.d.; resampling test (j-m), two-tailed Mann-Whitney *U* test (p); *P≤0.05, ***P≤0.001, ****P≤0.0001; n = 42 (a, real combination), 600 (a, inferred combination; b, inferred combination), 94 (b, real combination), 16 (c, real combination), 570 (c, inferred combination), 43 (p, cell cluster) clusters, 600 (o) angles, 44 (p, single cell) cells. Statistics and reproducibility are in the source data and Methods.

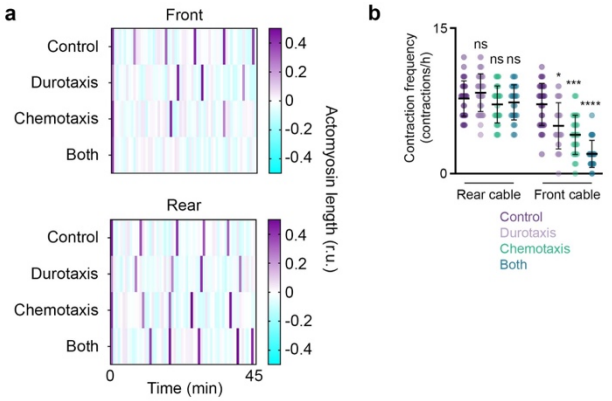

Extended Data Figure 10. Chemotaxis and Durotaxis synergically control actomyosin contraction polarity. a, Heat maps derived from the change in actomyosin cable length. Actomyosin contraction pulses are cyan/purple rectangles. Note that front contractions are inhibited when clusters are exposed to chemical and mechanical gradients. **b,** Quantification of the frequency of actomyosin contractions at the rear and front of cell clusters in control (purple), durotaxis (lilac), chemotaxis (green) and both (blue). Thick bars represent mean (b); error bars represent s.d. (b); Dunn's test (b); ns, $P>0.05$, *$P\leq0.05$, ***$P\leq0.001$, ****$P\leq0.0001$; n = 32 (b, control rear), 35 (b, control front), 41 (b, durotaxis rear), 26 (b, durotaxis front), 29 (b, chemotaxis rear), 28 (b, chemotaxis front), 25 (b, both rear), 26 (b, both front) clusters. Statistics and reproducibility are in the source data and Methods.